

## CHAPTER 3

---

# The LHC and the ATLAS detector

---

The Large Hadron Collider (LHC) and ATLAS detector are described. The LHC is among the largest scientific facilities in the history of humanity. It smashes more protons, at higher speeds, than any previous physics experiment. The ATLAS detector records these collisions and translates detector signals into physics phenomena. These are the experimental apparatuses which provide data for this thesis.

### 3.1 The LHC

The Large Hadron Collider (LHC) [36] is the most powerful particle accelerator ever built. It was first conceived in the 1980s with the purpose of finding the Higgs boson and discovering physics beyond our current understanding. It became operational in the early 2010s.

The LHC is a circular hadron collider 27 kilometers in circumference and 100 meters underground, near Geneva, Switzerland. It straddles the border of Switzerland and France. It is operated by the European Organization for Nuclear Research (CERN<sup>1</sup>) and occupies the underground tunnel originally constructed for the Large Electron Positron collider (LEP) for use in the 1990s. The construction costs of the LHC are approximately five billion USD.

The LHC collides hadrons at high energies to probe the boundaries of our understanding of particle physics. These collisions are observed by four major experiments situated along the LHC ring: ATLAS [37], CMS [38], ALICE [39], and LHCb [40]. ATLAS and CMS are general purpose particle detector experiments built for discovering physics of and beyond the Standard Model. ALICE is designed to observe heavy ion (lead nuclei) collisions and study the physics of quark-gluon plasma. LHCb specializes in the study of *b*-hadrons. An aerial view of the experiments is shown in Fig. 3.1.

---

<sup>1</sup>Conseil Européen pour la Recherche Nucléaire

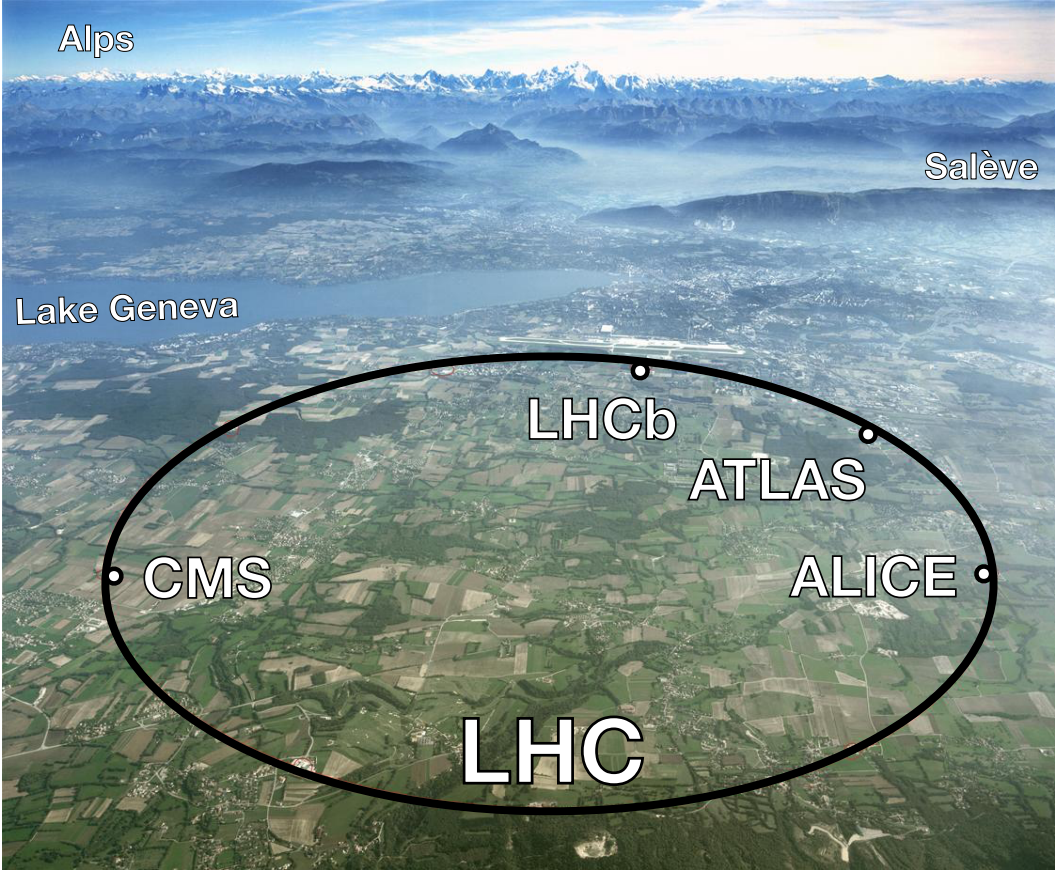


Figure 3.1: Aerial view of Geneva with an overlaid drawing of the LHC and associated experiments [41].

### 3.1.1 Specifications

The LHC is last step of a multi-stage chain of accelerators called the LHC accelerator complex [42], shown in Fig. 3.2. Protons are first retrieved from hydrogen atoms and accelerated by the Linac 2 linear accelerator to 50 MeV per proton. The protons are then passed successively to the Proton Synchotron Booster (PSB), Proton Synchotron (PS), and Super Proton Synchrotron (SPS) where they are accelerated to 1.4 GeV, 25 GeV, and 450 GeV, respectively. The protons are finally fed into the LHC where they are maximally accelerated to 4 TeV in 2012 operations, yielding a center-of-mass collision energy of 8 TeV. This chain is summarized in Table 3.1. At full energy, the protons will typically circulate the LHC for many hours at a time.

Protons travel around the LHC in two oppositely circulated beams. The proton beams are bent and focused by powerful superconducting electromagnets, which operate cryogenically at an ultracold

### 3. THE LHC AND THE ATLAS DETECTOR

---

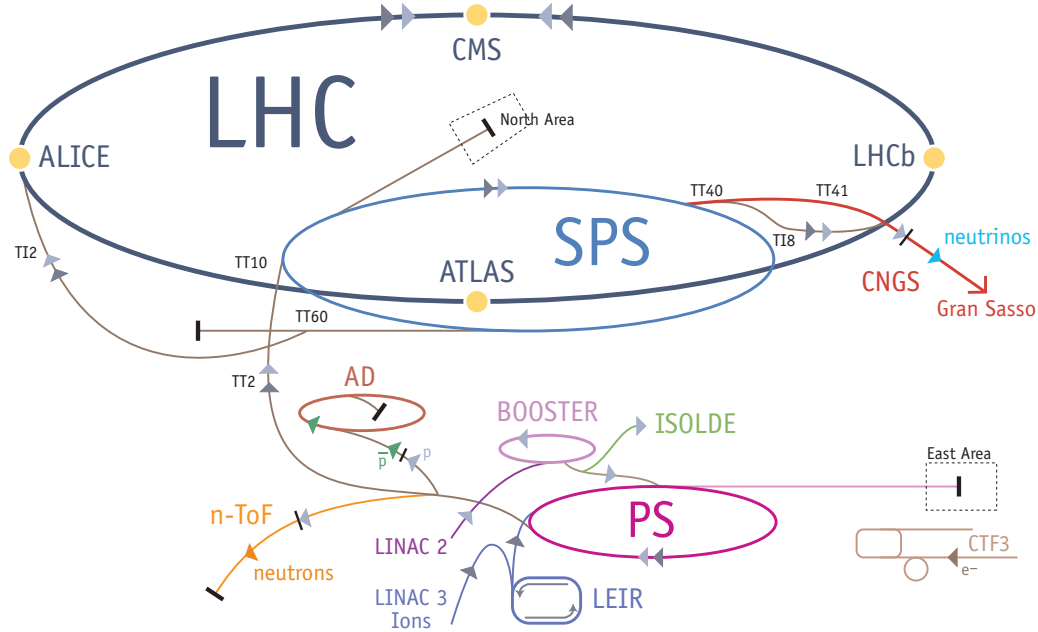


Figure 3.2: The LHC accelerator complex. Before reaching the LHC, protons are accelerated at Linac 2, the Proton Synchrotron Booster (PSB), the Proton Synchrotron (PS), and the Super Proton Synchrotron (SPS) [43].

Table 3.1: The accelerators of the LHC accelerator chain and the speed at which they accelerate protons in 2012. [43].

proton energy (GeV)	speed of light (%)	accelerator
0.05	31.4	Linac 2
1.4	91.6	PSB
25	99.93	PS
450	99.9998	SPS
4000	99.99997	LHC

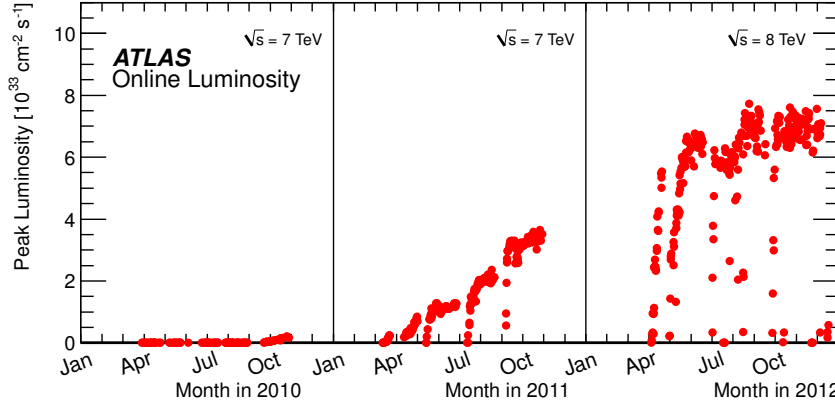


Figure 3.3: The peak luminosity as measured in different data-taking periods [46]. The peak Run-I luminosity is  $0.8 \times 10^{34} \text{cm}^{-2}\text{s}^{-1}$ .

temperature of 2 K (-456 F). The proton beams are segmented into groups of protons called *bunches*. Each beam contains 2808 bunches, and each bunch contains approximately  $10^{11}$  protons. Many protons are included per bunch to maximize the probability of a proton-proton collision for a given bunch crossing. A bunch crossing happens every 50 nanoseconds during operations in 2012.

### 3.1.2 Operations

The LHC is designed to collide protons with a center-of-mass energy  $\sqrt{s}$  of 14 TeV and an instantaneous luminosity of  $10^{34} \text{cm}^{-2}\text{s}^{-1}$ . However, while commissioning in 2008, the machine broke due to a faulty electrical connection between two superconducting magnets [44]. The LHC was repaired in 2009 and, to ensure safer operation, began colliding protons below design energy and instantaneous luminosity in late 2009.

The LHC collided protons for physics studies in 2010-2012 at a reduced energy of 7 TeV (2010-2011) and 8 TeV (2012). These years of data-taking are referred to as *Run-I* and include the discovery of the Higgs boson. The peak instantaneous luminosity achieved was  $7.7 \times 10^{33} \text{cm}^{-2}\text{s}^{-1}$  in 2012 [45], which doubled the peak luminosity of 2011 data-taking.

To increase the number of collisions recorded, many proton collisions are allowed to occur within a single bunch crossing. This average number of proton collisions per bunch crossing  $\langle\mu\rangle$  is referred to as *pileup*. The average  $\langle\mu\rangle$  in 2012 is around 20 collisions per crossing and reaches as large as 35-40. Profiles of the pileup are shown in Figs. 3.3 and 3.4.

The LHC, ATLAS, and CMS are undergoing maintenance and upgrades from early 2013 until early 2015. Data-taking is intended to resume in mid-2015 with an increased  $\sqrt{s} = 13$  TeV and a

### 3. THE LHC AND THE ATLAS DETECTOR

---

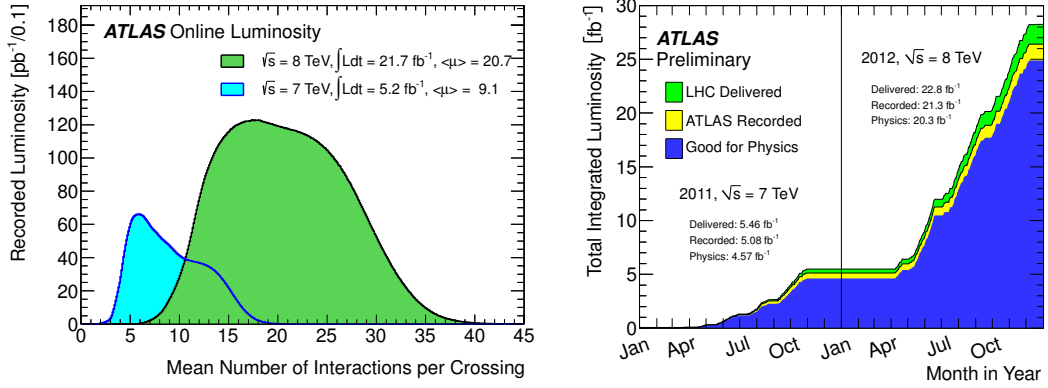


Figure 3.4: Distributions of the recorded luminosity in bins of  $\langle \mu \rangle$  (left) and the total integrated luminosity as a function of time (right) [46]. In 2011 (2012), the average  $\langle \mu \rangle$  is 9.1 (20.7) and the total integrated luminosity for physics analysis is  $4.6 \text{ fb}^{-1}$ . ( $20.3 \text{ fb}^{-1}$ ).

instantaneous luminosity of  $10^{34} \text{ cm}^{-2} \text{ s}^{-1}$ . The *Run-II* data-taking campaign is intended to last for the next three to four years, until 2017-2018, when another round of upgrades are planned to be installed.

These datasets allow the ATLAS and CMS experiments to probe physics of the Standard Model and beyond unlike any previous experiment in particle physics. Despite operating below design energy and luminosity, the Run-I dataset accesses electroweak processes at unprecedented rates, as shown in Fig. 3.5. This rate will increase again in the Run-II data-taking campaign, thereby offering a new opportunity for discovery.

## 3.2 The ATLAS detector

The ATLAS<sup>2</sup> detector is a general purpose cylindrical detector centered on one of the LHC collision points. It is 46 meters in length, 25 meters in diameter, and weighs 7000 tons. Assembly began at CERN in 2003 and was completed in 2008. A schematic rendering is shown in Fig. 3.6.

ATLAS is built to measure and classify particles arising from proton-proton collisions. These particles can be as low energy as a few hundred MeV to as high energy as multiple TeV. To detect such a broad range of phenomena, multiple subdetectors are employed. These are concentric about the proton-proton interaction point (IP) and are designed to observe different classes of particles.

The *inner detector* is closest to the beams and is designed to detect charged particles. The *calorimeters* are outside the inner detector and are designed to stop all particles except muons and

---

<sup>2</sup>A Toroidal LHC Apparatus

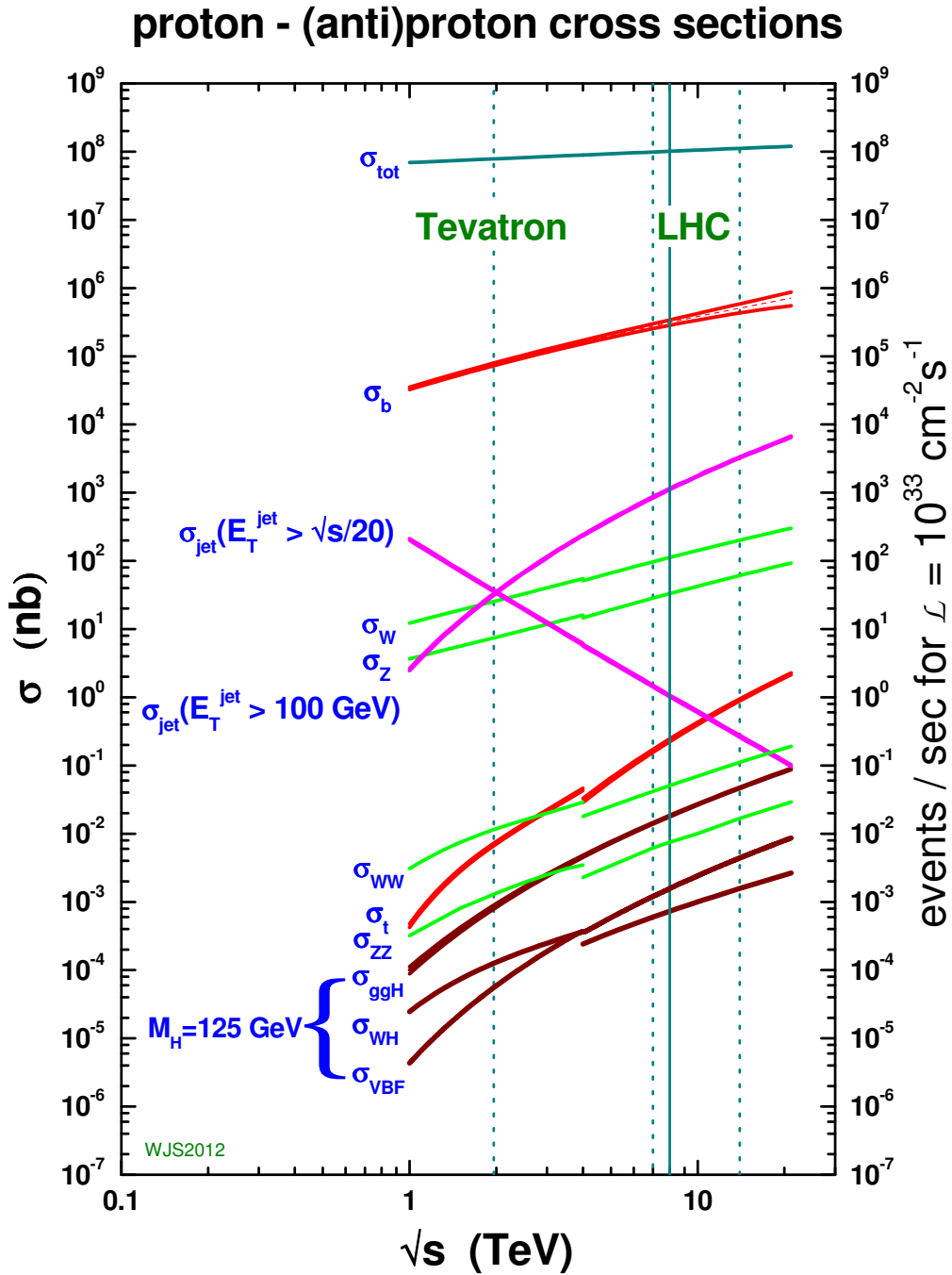


Figure 3.5: Cross sections for  $p p$  and  $p \bar{p}$  processes in the center-of-mass energy regime relevant to the Tevatron and LHC, courtesy of W.J. Stirling [47].

### 3. THE LHC AND THE ATLAS DETECTOR

---

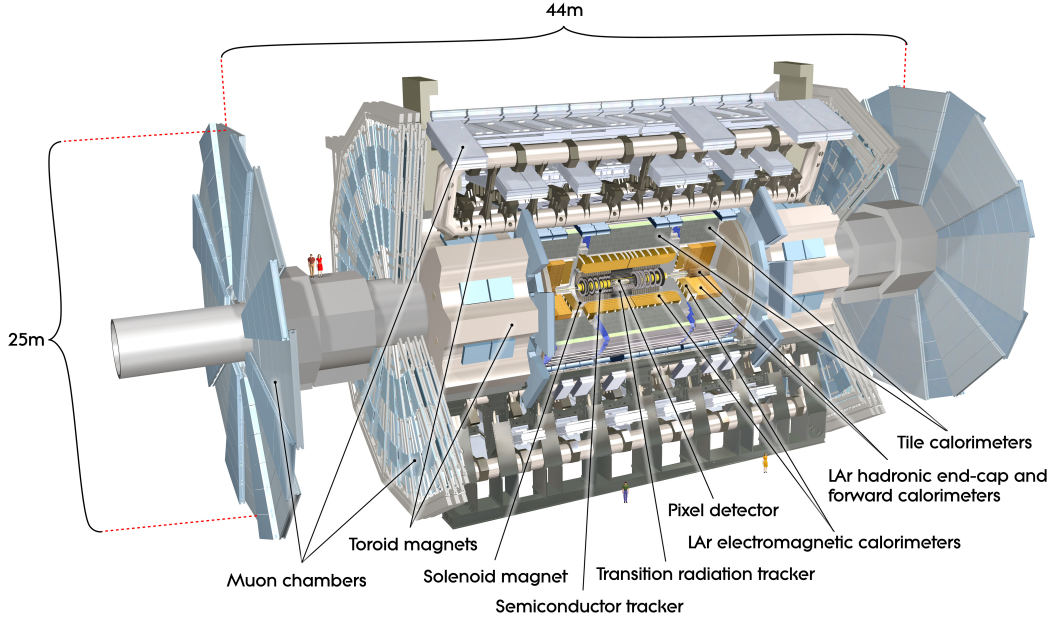


Figure 3.6: Scale rendering of the ATLAS detector with the various subdetectors highlighted [48].

neutrinos. The *muon system* is furthest from the beams and is designed to detect muons as they exit ATLAS.

The inner detector is enclosed by a solenoidal magnet with a field of approximately 2 Tesla. A large toroidal magnet exists within the muon system which has a field of 2 to 8 Tesla. The purpose of these magnets is to bend the trajectory of charged particles as they travel through ATLAS. The momenta of these particles can then be precisely inferred from the measured trajectory according to the classical Lorentz force law.

ATLAS uses a right-handed coordinate system with its origin at the IP in the center of the detector, and the  $z$ -axis along the beam line. The  $x$ -axis points from the IP to the center of the LHC ring, and the  $y$ -axis points upwards. Cylindrical coordinates  $(r, \phi)$  are used in the transverse plane,  $\phi$  being the azimuthal angle around the beam line. The pseudorapidity  $\eta$  is typically used in place of the polar angle  $\theta$  and is defined as  $\eta = -\ln(\tan \frac{\theta}{2})$  [29].

The ATLAS collaboration was formed in 1992, and as of 2011, it includes over 3000 scientists from 174 institutions and 38 countries. It is one of the largest scientific collaborations in the world.

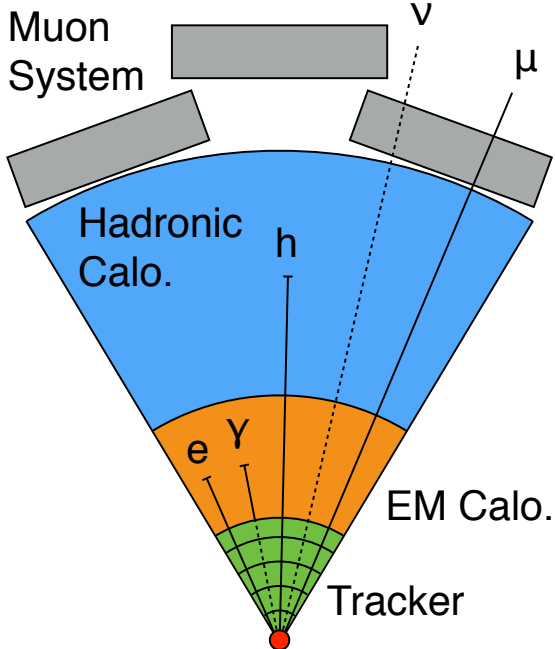


Figure 3.7: Transverse schematic view of a wedge of the ATLAS detector. Charged particles leave tracks in the tracker, electrons and photons typically stop in the electromagnetic calorimeter, hadrons like charged pions typically stop in the hadronic calorimeter, and muons are tagged by the muon system as they exit. Neutrinos escape undetected.

### 3.2.1 Inner detector and tracking

The inner detector (ID), also called the *tracker*, is designed to precisely measure the trajectory and momentum of charged particles as they pass through the 2 T magnetic field provided by the solenoid, such as electrons, muons, and charged pions [37]. The ID is composed of three independent but complementary subdetectors: the Pixel detector, the Semiconductor Tracker (SCT), and the Transition Radiation Tracker (TRT). These are shown in Fig. 3.8. The subdetectors are split into barrel and endcap components, have full  $2\pi$  coverage in  $\phi$ , and have at least coverage in  $|\eta|$  up to 2.0. Information from all three subdetectors is used to reconstruct tracks and vertices.

#### 3.2.1.1 Subdetectors

The Pixel detector exists closest to the interaction point and employs three layers of silicon pixels [37]. The pixels have fine granularity and are designed to deliver precise measurement of tracking parameters close to the IP, which are useful for secondary vertexing. The intrinsic resolution of the pixels in the barrel are  $10 \mu\text{m}$  in  $r\phi$  and  $115 \mu\text{m}$  in  $z$ . The Pixel detector has  $80 \times 10^6$  channels, by far the

### 3. THE LHC AND THE ATLAS DETECTOR

---

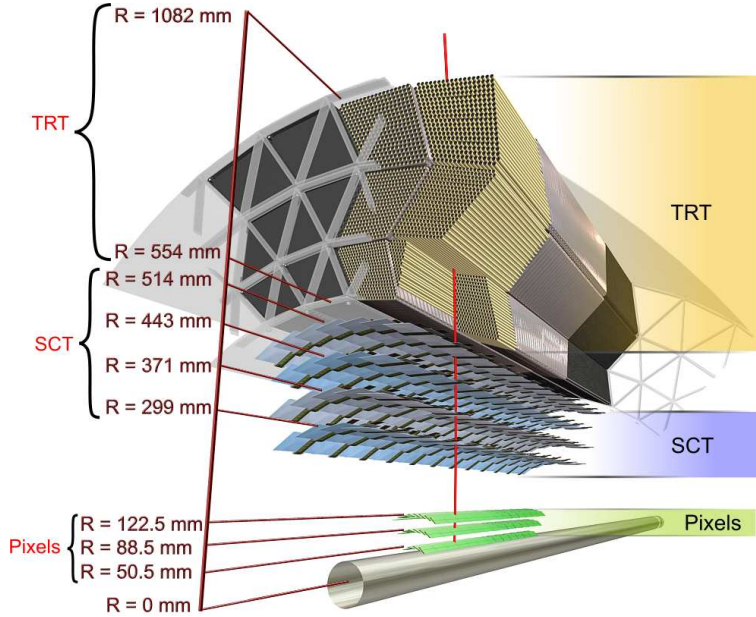


Figure 3.8: A diagram of the barrel of the Inner Detector: the three layers in the Pixels, the four layers in the SCT, and the many layers of the TRT [49].

most of any ATLAS subdetector, and usually provides three measurements per charged particle. The track resolution is  $10 \mu\text{m}$ . The Pixel detector has coverage up to  $|\eta| = 2.5$ .

The SCT surrounds the Pixel detector and also employs silicon detector elements, using microstrips instead of pixels [37]. The strips are arranged in four double layers, with the pairs arranged at small angles relative to each other, to make a three-dimensional measurement. The intrinsic resolution of the strips in the barrel are  $17 \mu\text{m}$  in  $r\phi$  and  $580 \mu\text{m}$  in  $z$ . The SCT has  $6.3 \times 10^6$  channels and usually provides eight measurements per charged particle. It has coverage up to  $|\eta| = 2.5$ .

The TRT surrounds the SCT and is the largest of the ID subdetectors [37]. It employs 300,000 straw drift tubes for recording the passage of charged particles. The intrinsic resolution of the TRT in the barrel is  $130 \mu\text{m}$  in  $r\phi$ ; the drift tubes cannot make a measurement in  $z$ . The TRT has 350,000 channels and usually provides 30 or more measurements per charged particle. It has coverage up to  $|\eta| = 2.0$ . A comparison of subdetector features is shown in Table 3.2.

The TRT additionally provides information for classifying charged particles as electrons or pions via the detection of transition radiation in the xenon gas mixture in the drift tubes [50]. This radiation is produced when a charged particle crosses the boundary between two media of different dielectric constants and is proportional to the Lorentz  $\gamma$  of a particle. For an electron and charged pion of equal

### 3. THE LHC AND THE ATLAS DETECTOR

---

momentum, the electron is therefore much more likely to produce TR than the pion since its mass is 200 times smaller. Transition radiation is observed in the TRT as hits well above the threshold for tracking, which are referred to as *high threshold* hits, as opposed to *low threshold*.

#### 3.2.1.2 Tracking

Information from these three subdetectors are combined to make *tracks*, which have a unique correspondence to charged particles and are meant to describe their trajectory and momentum. As a charged particle travels through the ID, it leaves *hits* in each subdetector along its trajectory, as shown in Fig. 3.9. These are built into tracks with a three-dimensional fit using Kalman filtering tools which can account for multiple scattering as the charged particle traverses the media of the ID [49, 51]. The ATLAS tracking algorithms builds tracks for charged particles as low momentum as a few hundred MeV.

A vertex reconstruction algorithm [53, 51] is used to determine if multiple tracks originate from a single  $pp$  collision. The output of the algorithm is a complete set of vertices per event and the association of each track to a vertex. Starting with the set of all tracks passing simple goodness criteria (e.g., requiring a minimum number of hits in the silicon detectors), a vertex seed is derived from the global maximum of  $z$  coordinates, and tracks are associated to that seed using a  $\chi^2$  fitting algorithm. Tracks incompatible with the vertex are then used as seeds for the next iteration of the vertexing algorithm until all tracks are exhausted.

Vertexing is essential for deciding which tracks (and thus physics objects) originate from the  $pp$  collision of interest and which tracks do not. The vertex associated to the collision of interest is called the *primary vertex* and is conventionally the vertex with the highest track  $p_T^2$  associated to it. If a track is not consistent with having been produced in the primary vertex, it is typically ignored as originating from a pileup interaction. This is the best and most intuitive method of ignoring pileup contributions since the calorimeter cannot extrapolate particle trajectories back to the beamline with nearly as good precision. A visualization of the power of tracking for pileup rejection is shown in Fig. 3.10.

Table 3.2: Features of the subdetectors in the barrel of the Inner Detector: the Pixel detector, the SCT, and the TRT [49].

Subdetector	Channels	Element size [ $\mu\text{m}$ ]	Resolution [ $\mu\text{m}$ ]	Layer radii [mm]
Pixels	$80 \times 10^6$	$50 \times 400$	$10 \times 115$	50.5, 88.5, 122.5
SCT	$6.3 \times 10^6$	$80 \times 120000$	$17 \times 580$	299, 371, 443, 514
TRT	$350 \times 10^3$	4000	$130 \times \emptyset$	554 – 1082

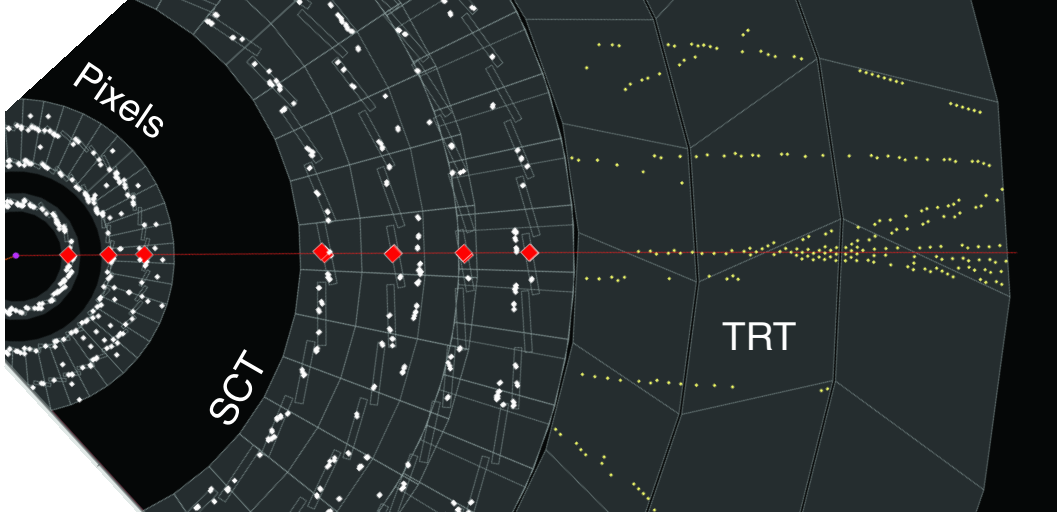


Figure 3.9: Event display of a charged particle traveling, from left to right, through three layers of the Pixels detector, four layers of the SCT, and many layers of the TRT [52]. The particle undergoes a material interaction in the TRT and produces multiple additional particles.

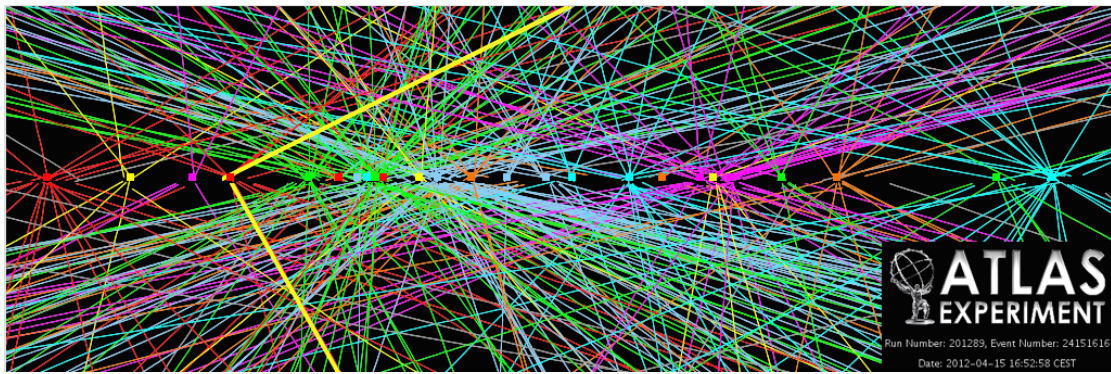


Figure 3.10: Event display of a  $Z \rightarrow \mu\mu$  event with 25 reconstructed vertices in 2012 data-taking [54].

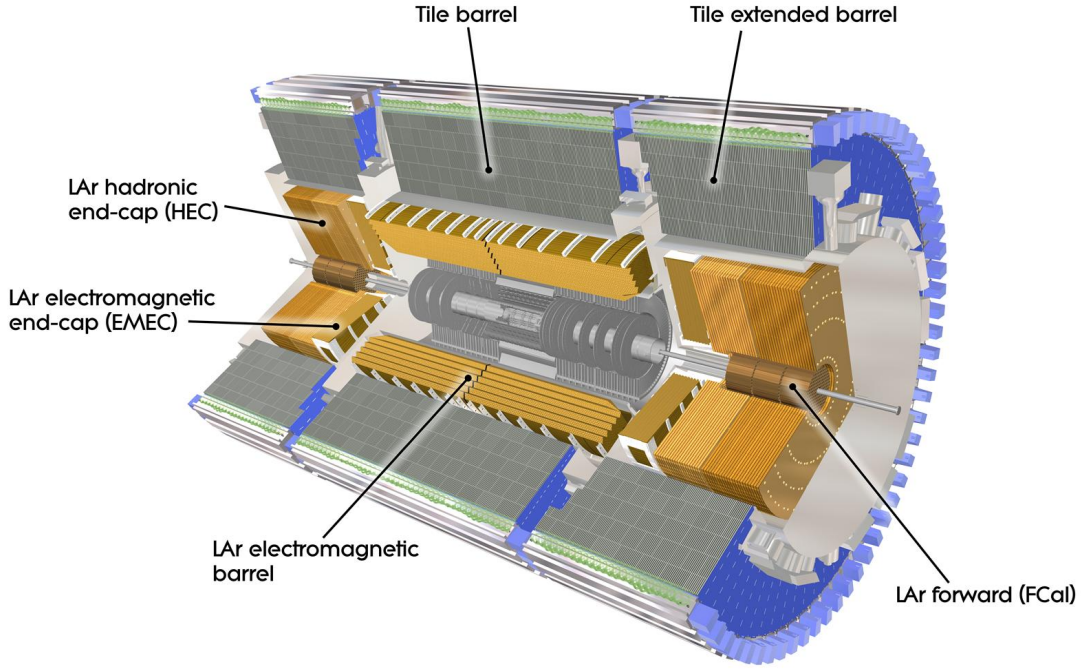


Figure 3.11: A diagram of the ATLAS calorimeters [37].

A track can then be described by five parameters: the transverse impact parameter relative to the primary vertex  $d_0$ , the longitudinal impact parameter  $z_0$ , the azimuthal angle  $\phi_0$ , the polar angle  $\theta$ , and the ratio of charge to momentum  $q/p$ .

### 3.2.2 Calorimeters and clustering

The ATLAS calorimeters sit outside the inner detector and the solenoid magnet. They are designed to stop particles like electrons, photons, and pions and to measure their energy. The calorimeters are grouped into electromagnetic (EM) and hadronic calorimeters, where the name describes the class of particle they are designed to stop. Both classes of calorimeters are *sampling* calorimeters, meaning only a fraction of a particle shower energy is observed, and the full shower energy must be inferred. Dense absorber material is used to initiate showers, and interleaved active material is used for detecting the showers.

The calorimeter subdetectors are shown in Fig. 3.11. They are split into barrel and endcap components, have full  $2\pi$  coverage in  $\phi$ , and have coverage in  $|\eta|$  up to 4.9. Information from all subdetectors is used to reconstruct calorimeter clusters.

### 3.2.2.1 Subdetectors

The EM calorimeters are subdivided into barrel and endcap components, which cover  $|\eta| < 1.5$  and  $1.4 < |\eta| < 3.2$ . An additional presampler exists for  $|\eta| < 1.8$  to account for showers starting before the calorimeter. Lead plates are used as the absorber material with liquid argon (LAr) as the active material. An accordion-style geometry is employed for uniform  $\phi$  coverage without azimuthal cracks. The EM calorimeter is radially subdivided into first, second, and third layers away from the beamline. The first and second layers are finely segmented in  $\eta$  for providing detailed descriptions of shower shapes, which are important for particle identification algorithms. The second layer is also the largest layer and usually contains most of the energy of an electromagnetic shower. The third layer measures the leftover energy which is not deposited in the first or second layers.

The hadronic calorimeter is also subdivided into barrel and endcap components. The barrel tile calorimeter uses steel as the absorber material and scintillating tiles as the active material, and it covers the range  $|\eta| < 1.7$ . The endcap calorimeter uses copper plates as the absorber material and LAr as the active material, and it covers the range  $1.5 < |\eta| < 3.2$ . The hadronic calorimeters are significantly coarser than the EM calorimeter because electrons and photons typically do not reach the hadronic calorimeters, hence particle identification techniques are less valuable.

Finally, the forward calorimeter (FCal) covers the very forward region  $3.1 < |\eta| < 4.9$  and uses LAr as active material. It is typically grouped with the hadronic calorimeters since the identification of electromagnetic objects stops at the boundary of the inner detector ( $|\eta| < 2.5$ ), hence the FCal is most often used in measuring the energy of hadrons.

### 3.2.2.2 Clustering

EM objects, such as photons and electrons, tend to produce narrow calorimeter showers which are dominantly contained in the EM calorimeters. Hadrons, such as charged pions, tend to produce broader showers and travel through the EM calorimeters and deep into the hadronic calorimeters before stopping. Hadronic showers can also include significant EM deposits from neutral pions which decay to two photons before reaching the calorimeters. A comparison of electron and pion showers is shown in Fig. 3.12. All particles leave a signature of large deposits in adjacent calorimeter cells.

Calorimeter cells from all subdetectors are combined into higher level objects by a three-dimensional topological clustering algorithm [56]. The algorithm uses the iterative 4-2-0 scheme: first, cluster seeds are built from any cell with more than  $4\times$  larger deposit than expected from noise. Second, any cell neighboring a seed cell with more than  $2\times$  larger deposit than noise is added to the cluster. Last, any cell neighboring the existing cluster with more than  $0\times$  larger deposit than noise is added.

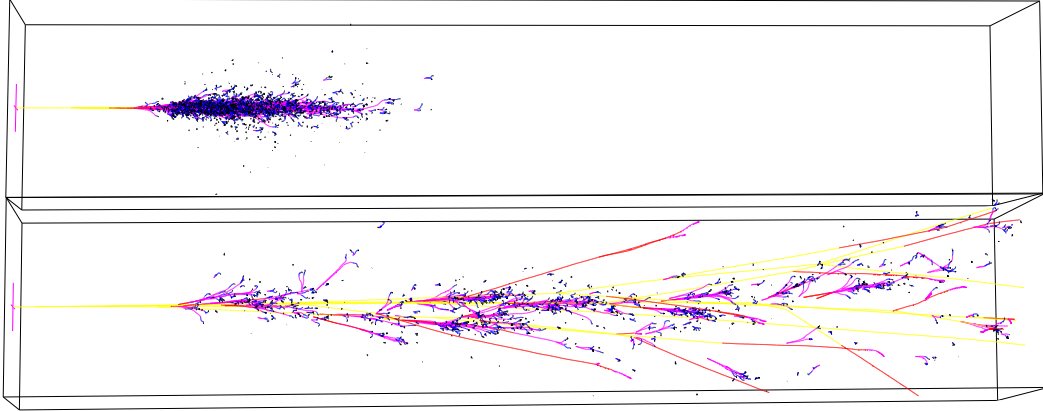


Figure 3.12: Display of simulated electron (top) and charged pion (bottom) showers, where both particles are 50 GeV and pass through iron [55].

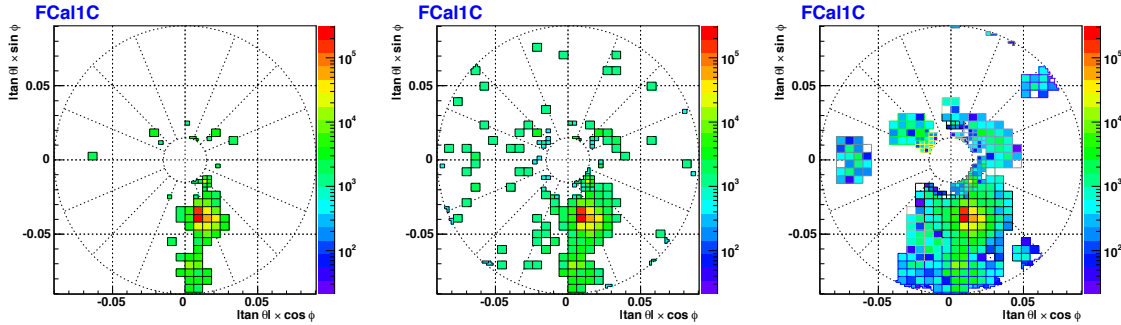


Figure 3.13: Event display of a jet in the forward calorimeter with cell energies greater than  $4\sigma_{\text{noise}}$  (left),  $2\sigma_{\text{noise}}$  (center), and with the 4-2-0 topological clustering algorithm [57].

Another clustering algorithm, called the *sliding window* algorithm, is used specially for EM objects. The sliding window algorithm uses a small, rectangular tower window to seed clusters in the EM calorimeter since EM objects tend to produce predictably narrow showers.

### 3.2.3 Muon spectrometry

The muon system (MS), also called the *muon spectrometer*, is designed to measure the trajectory and momentum of muons [58], especially at high  $p_T$ . It is furthest from the interaction point, and muons with less than a few GeV of momentum are unable to reach the MS before looping back into the detector due to barrel and endcap toroid magnets, which provide a magnetic field between 2 and 8 Tesla. It detects muons in the same style as the Inner Detector wherein the trajectory of charged

### 3. THE LHC AND THE ATLAS DETECTOR

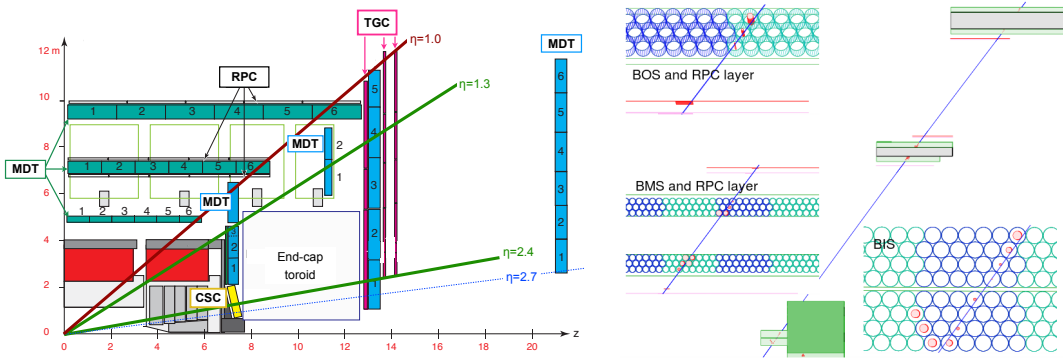


Figure 3.14: A diagram of the ATLAS muon system (left) [59] and a display of a muon candidate passing through three layers of the RPCs and MDTs (right) [54].

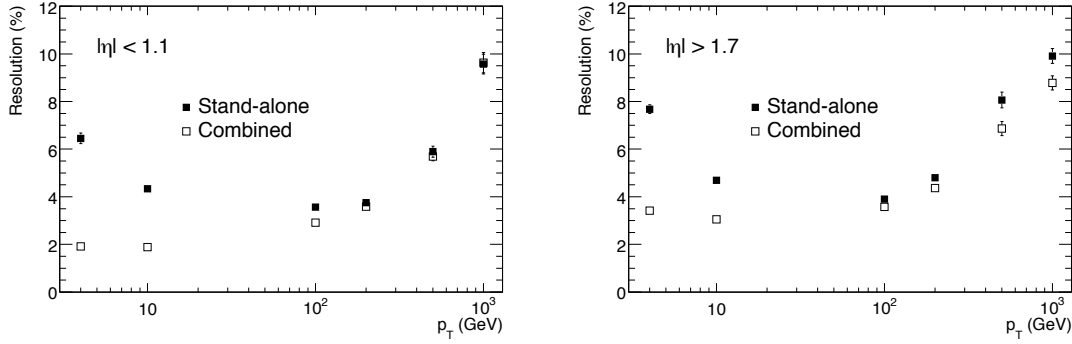


Figure 3.15: Muon momentum resolution for  $|\eta| < 1.1$  (left) and  $|\eta| > 1.7$  (right) for the stand-alone MS and the combination of the MS and inner detector [37].

particles can be traced through the MS and the momentum can be inferred from the track curvature.

The MS is comprised of four subdetectors: the Monitored Drift Tubes (MDTs), the Cathode Strip Chambers (CSCs), the Resistive Plate Chambers (RPCs), and the Thin Gap Chambers (TGCs), as shown in Fig. 3.14. The MDTs are used for precision measurements of the muon trajectory and momentum, and are used for the full range of the MS,  $|\eta| < 2.7$ . The CSCs are additionally deployed in the forward region  $|\eta| > 2.0$ . In the hardware trigger, where fast processing is required, the RPCs are used in the barrel and the TGCs are used in the endcap.

The MS and ID provide independent measurements of muon momenta. These measurements are combined for an overall measurement of muon momentum to exploit the advantages of each subdetector. The MS measurement dominates the combination at muon  $p_T$  in the hundreds of GeV and above, as shown in Fig. 3.15.

### 3.3 Particle identification

One of the major tasks in particle physics is the transformation of low-level detector outputs to high-level physics objects. At ATLAS, this is typically done in two steps referred to as *reconstruction*. First, detector outputs like inner detector hits and calorimeter cells are converted to tracks and clusters, respectively, as discussed previously. Second, combinations of tracks and clusters are converted into physics objects.

In addition to reconstruction, physics objects often require identification and calibration. Identification refers to the determination of which particle is responsible for a given detector signal, e.g., is a deposit in the calorimeter more likely to be from an electron or a charged pion. Calibration refers to the porting of a measured energy in the detector to the energy of a physics object. Calibration accounts for effects like pileup and dead material in the subdetectors.

These physics objects are often meant to exactly represent an individual particle, such as a muon. Otherwise, the physics objects represent a collection of particles which are naturally grouped together. For example, a *jet* represents the group of hadrons produced when a quark or gluon propagates through ATLAS.

#### 3.3.1 Muons

Muons are among the simplest physics objects to reconstruct since a large fraction of ATLAS is built specifically for this purpose. They are minimum ionizing particles and do not deposit significant energy in the calorimeters, hence they are the only particles expected to regularly reach and interact with the MS.

Muons are reconstructed by matching tracks in the MS to tracks in the ID [60], where track quality criteria are required in both subdetectors. This is  $\approx 99\%$  efficient for an inclusive collection of muons from  $Z \rightarrow \mu\mu$ , and it is limited by lack of coverage of the MS at  $|\eta| < 0.1$  and  $1.1 < \eta < 1.3$ . The performance of the muon calibration is shown in Fig. 3.16

Muons are most often used in ATLAS as the decay products of electroweak bosons like the  $W$  and  $Z$ . They are also produced in the decays of some hadrons, but muons from these processes can be rejected by requiring that the muon be isolated in the detector, both in the inner detector and in the calorimeters. Since the purity of muon reconstruction is already high, additional muon identification techniques are not explored.

### 3. THE LHC AND THE ATLAS DETECTOR

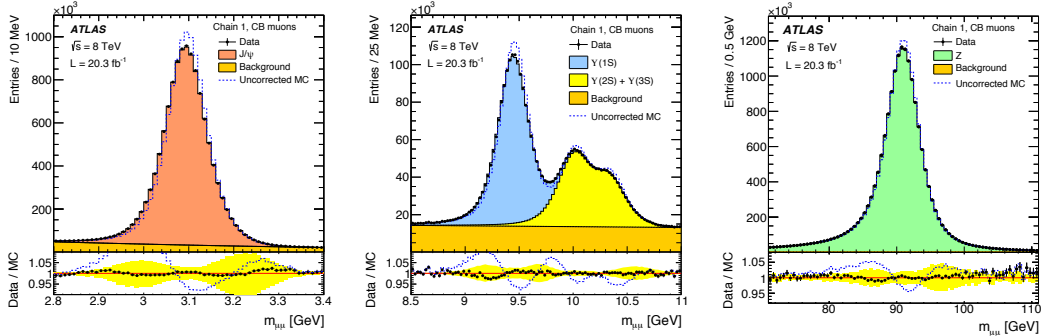


Figure 3.16: Validation of the muon energy scale corrections in  $J/\Psi$  events (left),  $\Upsilon$  events (center), and  $Z$  events (right) [60].

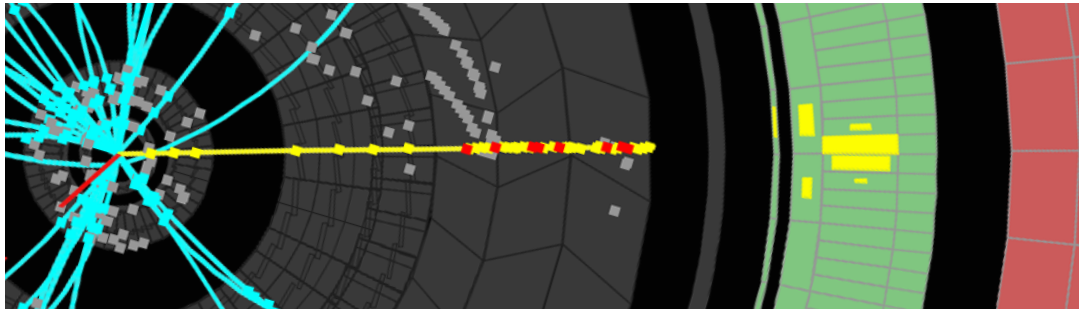


Figure 3.17: Display of an electron traversing the ID, leaving hits in the TRT consistent with transition radiation, and depositing a narrow cluster entirely contained in the EM calorimeter [54].

#### 3.3.2 Electrons and photons

Electrons are reconstructed by matching sliding window calorimeter clusters to ID tracks [61]. This offers no rejection against other charged particles, however, so identification algorithms are built which exploit discriminating features of electrons. Relative to backgrounds, electrons are more likely to leave longitudinally narrow calorimeter deposits in the EM calorimeter, deposit very little energy in the hadronic calorimeter, and be isolated in the ID and the EM calorimeter. Electrons are also more likely to have transition radiation in the TRT. These properties are shown in Fig. 3.17 and allow for huge rejection of backgrounds, as shown in Fig. 3.18.

Photons have similar detector signatures as electrons since their calorimeter deposits are also longitudinally narrow and expected to be contained within the EM calorimeter [62]. Identification algorithm are split into two categories: isolated photons which leave no hits in the ID, and photons which convert into pairs of electrons before reaching the calorimeter.

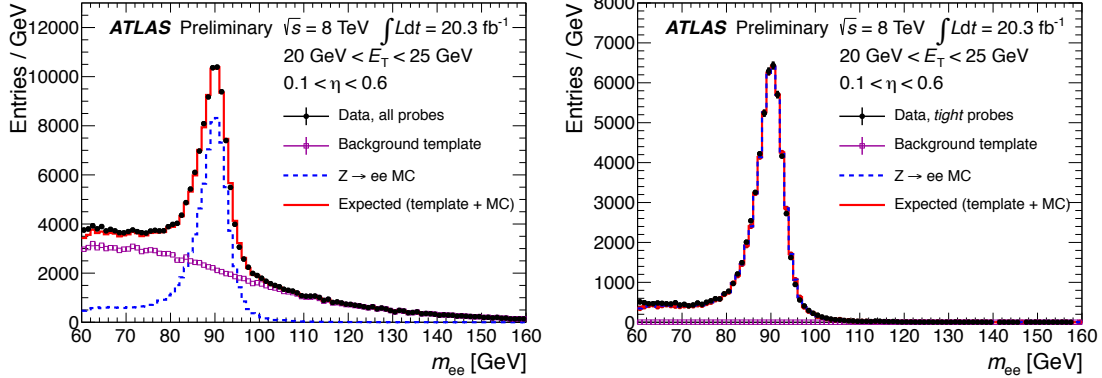


Figure 3.18: Data and predictions of  $m_{ee}$  before the electron identification algorithm is applied (left) and after (right) [61].

### 3.3.3 Hadrons

Instead of attempting to reconstruct individual hadrons, ATLAS reconstructs collimated sprays of hadrons referred to as jets [63]. Jet momenta range from  $\approx 10$  GeV to multiple TeV, and spatially they are the largest physics objects, though they can be as small as a single pion. Jets are produced copiously at hadron colliders, which can be problematic with significant pileup.

Jets are reconstructed from calorimeter topological clusters using the anti- $k_t$  algorithm [64] with a distance parameter of  $R = 0.4$ . This is an iterative clustering algorithm which groups topological clusters into jets based on their spatial proximity and momentum. Tracks can be associated to a jet based on simple spatial matching or the more robust ghost association [65]. A slew of corrections are applied to calibrate the energy and position of jets [63, 65]. These correct for effects like pileup, dead material, and the non-compensating nature of the calorimeters. Jets can additionally be classified as hard-scatter or pileup jets based on the fraction of their track momenta consistent with originating from the primary vertex [66].

Jets which arise from the fragmentation of  $b$ -quarks, referred to as  $b$ -jets, are given special treatment because the significant lifetime of  $B$ -hadrons means these jets can be distinguished from jets arising from lighter sources like gluons or  $u$ -quarks [67]. Multivariate algorithms are used to look for the signature of a second vertex with some spatial displacement from the primary vertex. An example of a displaced vertex, and the performance of these algorithms, are shown in Fig. 3.19.

Jets which arise from the hadronic decay of tau leptons are also treated specially because their signature in the detector can be distinguished from generic QCD jets. They are characteristically produced with 1 or 3 tracks and are relatively narrow objects in the ID and calorimeters [1]. They

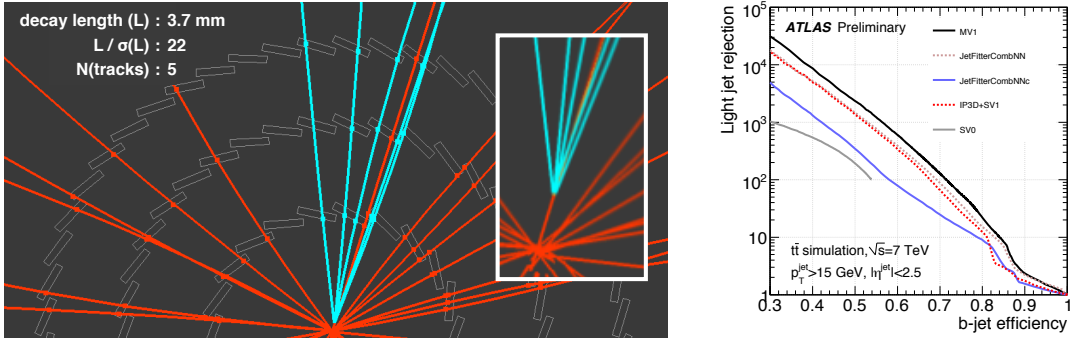


Figure 3.19: Event display of a displaced vertex consistent with the decay of a  $B$ -hadron (left) [68] and efficiency of  $b$ -jet identification algorithms measured in simulation as a function of light jet rejection (right) [69].

are discussed in greater detail in Section 4.3.

### 3.3.4 Neutrinos

Neutrinos do not interact with the ATLAS detector and escape undetected. But their presence can be inferred from momentum imbalance since each  $pp$  collision should conserve momentum. To measure the momentum imbalance, the negative total vector sum of momenta per collision is calculated, and the transverse projection the sum is interpreted to be the total transverse momentum of the neutrinos in the event. This is referred to as the missing transverse energy,  $E_T^{\text{miss}}$ .

The calculation of the total momenta in the event is done in two steps. First, the calibrated physics objects in the event, like jets and electrons, are collected and their vector sum is calculated. This is referred to as the *hard term* of the  $E_T^{\text{miss}}$  calculation. Second, tracks and calorimeter information unassociated to hard objects are combined and form the *soft term* of the  $E_T^{\text{miss}}$  calculation. The vector sum of the hard and soft terms is the total momentum imbalance of the event [70].

The soft term calculation is challenging because associating calorimeter information to a specific vertex is difficult in the presence of pileup. Hence multiple methods exist for calculating the soft term. A comparison of the  $E_T^{\text{miss}}$  resolution is shown in Fig. 3.20 as a function of the pileup of the event. Of the options available in 2014, the *STVF* method [71] has the best resolution. The STVF soft term is first calculated with calorimeter topoclusters, and the magnitude of the sum is then weighted down by the fraction of unassociated track momenta arising from the PV to the total unassociated track momenta of the event. This heavily suppresses the calorimeter-based soft term, which has a strong dependence on pileup.

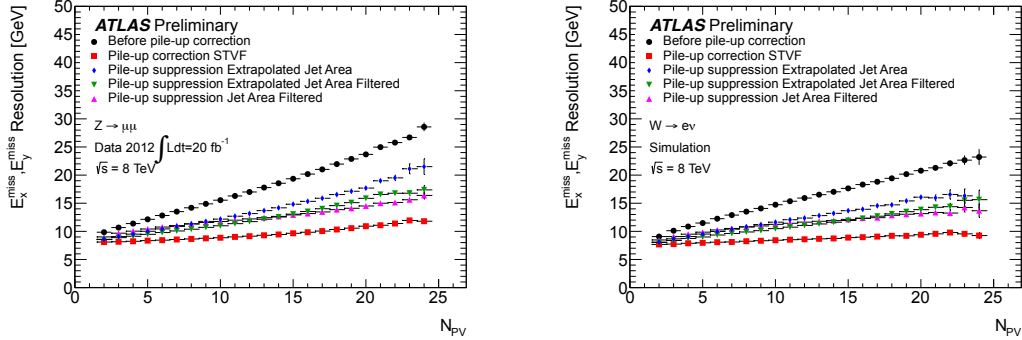


Figure 3.20: Resolution of various  $E_T^{\text{miss}}$  reconstruction algorithms as a function of the number of reconstructed primary vertices in  $Z \rightarrow \mu\mu$  events in data (left) and  $W \rightarrow e\nu$  events in simulation (right) [71].

### 3.4 Triggering

One of the most challenging aspects of physics at hadron colliders is that the vast majority of  $pp$  collisions produce low  $p_T$  QCD dijets, and these events are mostly uninteresting in searches for new physics. Additionally, ATLAS does not have the computing resources to reconstruct and save 20 MHz of  $pp$  collisions. A huge reduction of data is necessary immediately after the collisions occur. This reduction must be careful not to remove events with interesting signatures.

The scheme of fast reduction is called *triggering*. Reconstruction and decision-making in the trigger is referred to as occurring *online*, whereas the nominal ATLAS reconstruction occurs *offline*. The trigger is split into two stages. First, all  $pp$  collisions are sent to a hardware trigger with much coarser granularity than offline. Events passing the hardware trigger are then sent to software triggers with granularity comparable to offline. The hardware trigger is called *Level 1* (L1), and the software triggers are called the *High Level Trigger* (HLT). The HLT step is additional split into two stages, *Level 2* (L2) and *Event Filter* (EF). The reduction and latency targets are shown in Table 3.3.

Table 3.3: Approximate average trigger rates and latencies during 2012 data-taking [37, 59, 72].

system	input rate	output rate	reduction	latency
L1	20 MHz	70 kHz	300×	2.5 $\mu$ s
HLT, L2	70 kHz	5 kHz	15×	75 ms
HLT, EF	5 kHz	700 Hz	7×	1 s

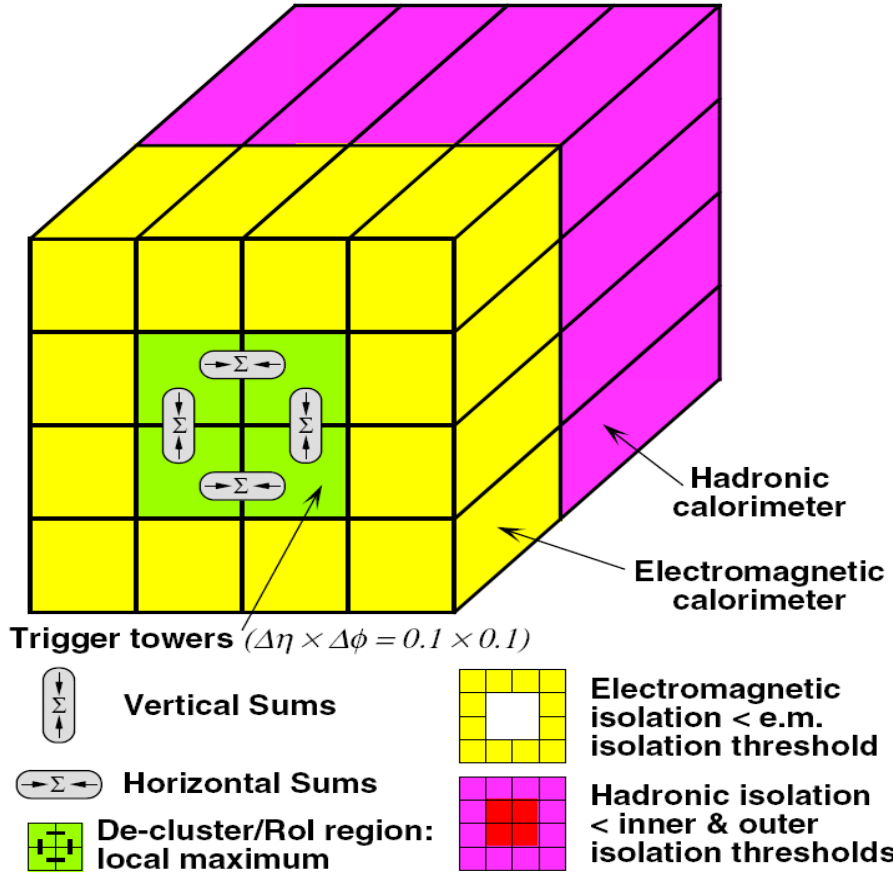


Figure 3.21: Schematic view of the calorimeter granularity available at the L1 trigger [73].

### 3.4.1 L1

The L1 trigger is the fastest and most reductive step of the trigger system. Only information from the calorimeter and muon subdetectors are available because the inner detector is not equipped to process events at tens of MHz, and because tracking algorithms are currently too slow. Performance is sacrificed for speed in the EM calorimeter and muon system: the granularity of the EM calorimeter is reduced for faster processing, as shown in Fig. 3.21, and only information from the RPCs and TGCs is read out from the muon system.

A consequence of the reduced granularity of the EM calorimeter is that the sophisticated offline identification algorithms cannot be used. For example, the only identification technique available for  $\tau_{\text{had}}$  at L1 is calorimeter isolation. Furthermore, the isolation can only be evaluated in a square annulus with the reduced granularity and cannot be  $p_T^{\text{L1}}$ -dependent.

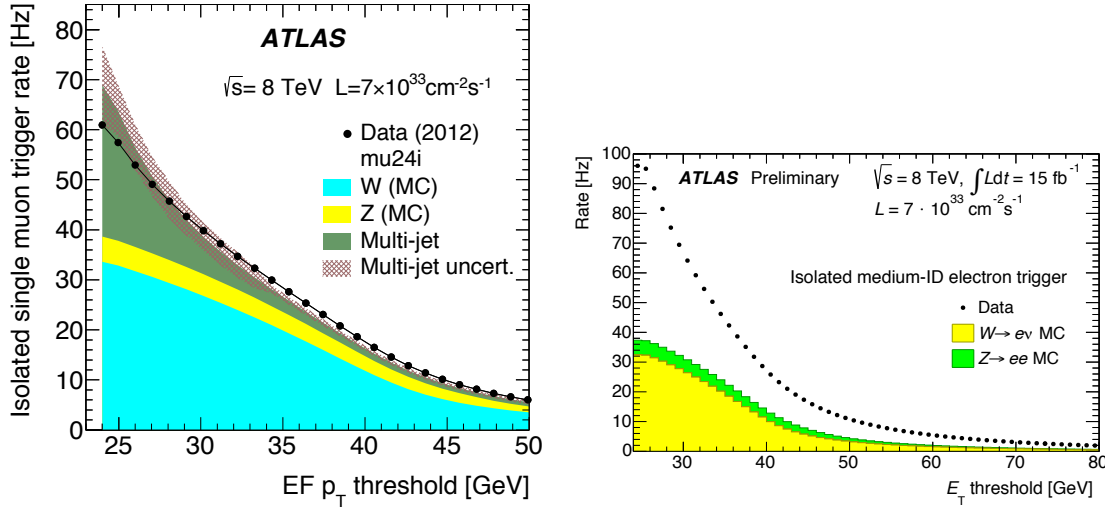


Figure 3.22: Trigger rate and predicted composition of the lowest unprescaled single muon trigger (left) [59] and single electron trigger (right) [74] in 2012 data-taking.

In Run-I, much of the L1 bandwidth is allocated to the inclusive single muon and single electron triggers. These are among the most used triggers in ATLAS physics and performance analyses because of their inclusiveness and because light leptons are characteristic of electroweak physics.

### 3.4.2 HLT

The HLT latency is much less restrictive than at L1. By the end of the HLT, tracking and topological clustering algorithms are run over a full scan and with the nominal granularity of the detector. Reconstruction, identification, and calibration algorithms closely resemble their offline counterparts, with adaptations to online made as necessary.

Like L1, much of the HLT bandwidth is allocated to the inclusive single muon and single electron triggers. The rate and predicted composition of these HLT triggers are shown in Fig. 3.22. Electrons and muons from  $W/Z$  decays are irreducible contributions to the HLT rate and are among the limiting factors.

## 3.5 Summary

The ATLAS physics program in Run-I of the LHC is a great success of detector operation, performance, and large-scale data analysis. ATLAS has measured cross-sections of processes ranging more than ten orders of magnitude, as shown in Fig. 3.23, including multiple production modes of the

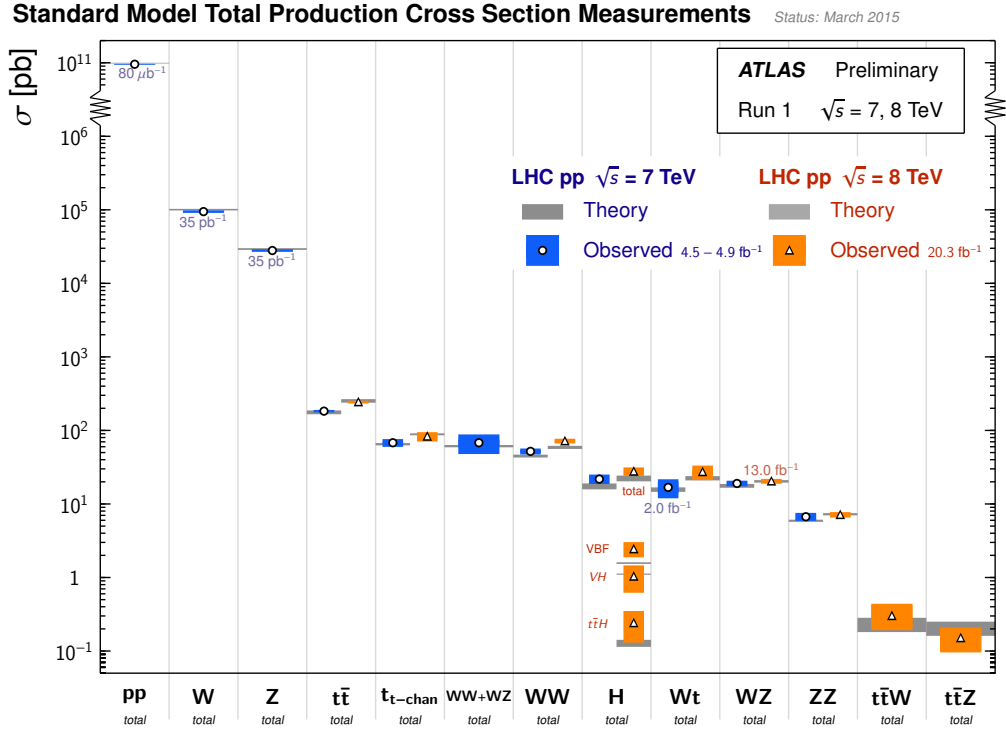


Figure 3.23: Summary of cross sections measured at ATLAS in 7 and 8 TeV data-taking [76].

recently discovered Higgs boson. As of early 2015, the ATLAS collaboration has authored more than 350 peer-reviewed publications [75].